Non-Spin-Echo 3D Transverse Hadamard Encoded Proton Spectroscopic Imaging in the Human Brain

Ouri Cohen,[1,2] Assaf Tal,[1] Gadi Goelman,[1,3] and Oded Gonen[1]*

A non-spin-echo multivoxel proton MR localization method based on three-dimensional transverse Hadamard spectroscopic imaging is introduced and demonstrated in a phantom and the human brain. Spatial encoding is achieved with three selective 90° radiofrequency pulses along perpendicular axes: The first two create a longitudinal $\pm M_Z$ Hadamard order in the volume of interest. The third pulse spatially Hadamard-encodes the $\pm M_Z$s in the volume of interest in the third direction while bringing them to the transverse plane to be acquired immediately. The approaching-ideal point spread function of Hadamard encoding and very short acquisition delay yield signal-to-noise-ratios of 20 ± 8, 23 ± 9, and 31 ± 10 for choline, creatine, and N-acetylaspartate in the human brain at 1.5 T from 1 cm^3 voxels in 21 min. The advantages of transverse Hadamard spectroscopic imaging are that unlike gradient (Fourier) phase-encoding: (i) the volume of interest does not need to be smaller than the field of view to prevent aliasing; (ii) the number of partitions in each direction can be small, 8, 4, or even 2 at no cost in point spread function; (iii) the volume of interest does not have to be contiguous; and (iv) the voxel profile depends on the available B_1 and pulse synthesis paradigm and can, therefore, at least theoretically, approach "ideal" "1" inside and "0" elsewhere. **Magn Reson Med 70:7–15, 2013. © 2012 Wiley Periodicals, Inc.**

Key words: brain; chemical shift imaging; Hadamard encoding; non-echo localized spectroscopy

INTRODUCTION

Magnetic resonance spectroscopic imaging (MRSI), also known as chemical shift imaging (CSI) (1,2), is commonly done using gradient phase encoding. Its most attractive advantages are its simplicity to implement, low specific absorption rate (SAR), and immunity to chemical shift displacement, making it also especially attractive at higher fields (3). However, CSI also has a few, often ignored limitations: its field of view (FOV) must be greater than the object to avoid aliasing and the finite k-space sampling, due to limited scan time, results in a sinc-like point spread function (PSF) that distributes

[1]Radiology Department, New York University, New York, New York, USA.
[2]Biomedical Engineering Department, Columbia University, New York, New York, USA.
[3]Human Biology Research Center, Hadassah Hebrew University Medical Center, Jerusalem, Israel.

*Correspondence to: Oded Gonen, Ph.D., Radiology Department, New York University School of Medicine, 660 First Avenue, 4th Floor, New York, NY 10016. E-mail: oded.gonen@med.NYU.edu

a fraction, per direction, of any voxel's signal across the FOV. Ignoring contributions from neighboring voxels, the net effect is a reduction in the localization accuracy (4–6) and an artifactual change of the signal-to-noise-ratio (SNR) (7). As the sensitivity and reasonable scan durations of protons at 1.5 T limits voxel size to ∼ 1 cm^3, the PSF at such low spatial resolutions admixes extraneous signals, especially from the skull lipids, into the volume of interest (VOI) that can confound and even overwhelm its metabolites' signals.

To avoid this extraneous contamination, these signals must be suppressed, e.g., by a series of outer volume suppression (OVS) bands over the skull (4,5). Although effective, the multitude of pulses entails high SAR. Nulling lipids with inversion recovery instead (6), may be less effective due to multiple T_1s and incurs a 30–40% SNR penalty (8). Either strategy is often combined with selective-excitation of a parallelepiped VOI using three orthogonal spatially selective radiofrequency (RF) pulses such as in stimulated echo acquisition mode (STEAM) or point-resolved-spectroscopy (9,10). Both incur two shortcomings: First, the common 30, 144, or 288 ms short, intermediate, or long echo times (TEs) (11–14) suffer 14–50% metabolites' signals T_2 decays. Second, TEs > 20 ms cause J-coupling modulation (15). Hybrid sequences that incorporate elements from both to overcome the obstacles either depend on echo formation with its T_2 signal loss (16), or require many OVS pulses that increase the SAR and recycle times (TR) (17).

These issues can be addressed with Hadamard spectroscopic imaging (HSI), which unlike CSI, offers a controlled PSF, regardless of the number of phase-encoding steps. Like CSI, HSI benefits from voxel-shift and zero-fill operations in postprocessing (18) and is also optimal in SNR/unit time since the entire VOI is excited each TR (19). Our goal in this article is to test two hypotheses: (i) HSI offers better localization, reflected by less signal "bleed"; and consequently, (ii) yields better voxel SNR than CSI by comparing the performance of a three-dimensional (3D) Transverse HSI (T-HSI) against 3D CSI in a phantom and in the brain of a healthy volunteer.

THEORY

T-HSI

T-HSI spatially encodes the relative "transverse" phase, ϕ_n^k, of the spins in the nth slice at either 0° or 180° according to the +1 or −1s of the kth row of an Nth order Hadamard matrix, $\mathbf{H}_N$ ($N = 2^n$ with n = 1, 2... integer) (19–21). This is repeated for each row of $\mathbf{H}_N$ as shown in Figure 1a. In matrix notation, HSI encoding along a direction, p (=X, Y, Z) is described as:
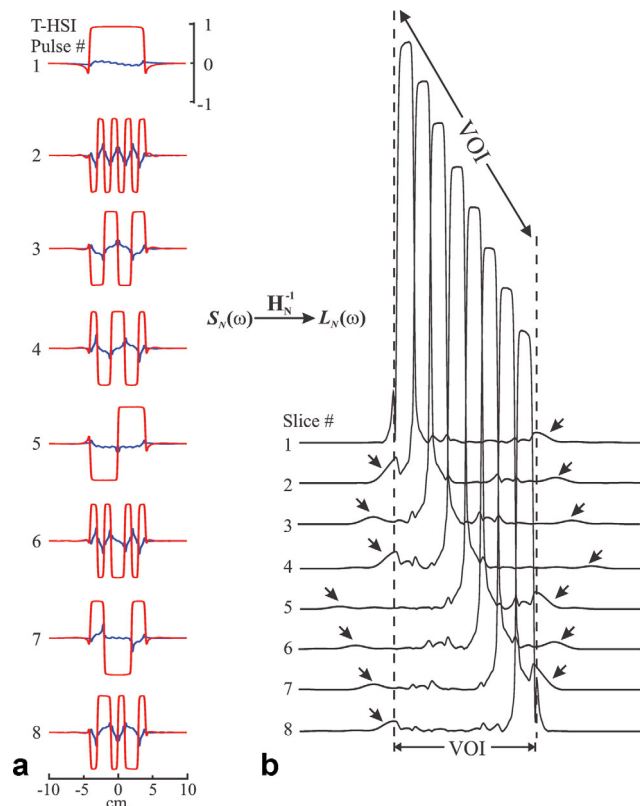
FIG. 1. M_x (red) and M_y (blue) transverse magnetization profiles for eighth-order T-HSI pulses obtained via simulation all on the same indicated $-1...1$ intensity and -10 to 10 cm scales (**a**) and voxel profiles resulting from Hadamard reconstruction of the eight signals (**b**). Pulse profile amplitudes vary according to the entries of the rows of the Hadamard matrix $\mathbf{H_N}$. Arrows indicate locations outside the VOI that are excited due to pulse imperfections. Imperfections inside the VOI have a minimal impact on the localization because of the small volume (under 1 cm^3) excited whereas those outside the VOI are handled using the OVS scheme and the Hadamard reconstruction as described in the text.

$\mathbf{H}_N \cdot L_p(t) = S_N(t)$ or after inverse Fourier transform :
$$\mathbf{H}_N \cdot L_p(\omega) = S_N(\omega) \tag{1}$$

The localized signals from the N slices, $L_p(t)$, shown in Figure 1, are obtained from the N observed signals, $S_N(t)$, by inverse Hadamard transform, i.e., multiplication by $\mathbf{H}_N^{-1} = \frac{1}{N}\mathbf{H}_N$ (22). To prevent T_1 modulation, T-HSI in more than one-dimension (1D) needs either a 90° flip angle or TR $\geq 5 \cdot T_1$ (20).

The Sequence

Spatial encoding begins with a selective $90°_x$ (lower-case subscripts indicate RF phases) T-HSI pulse, as shown in Figure 2. It converts $I_Z \rightarrow \pm I_Y$ where the $+/-$ reflect the transverse phase ϕ_n^k above, as shown in Figure 3. The $\pm I_Y$s evolve under the chemical-shift and resonance-offset Hamiltonian $-\Delta\omega I_Z$ and at time $\tau/2$ later become,

$$\pm I_Y \xrightarrow{-\Delta\omega \frac{\tau_1}{2} I_Z} \pm[I_Y\cos(\frac{\Delta\omega\tau_1}{2}) - I_X\sin(\frac{\Delta\omega\tau_1}{2})]. \tag{2}$$

If this evolution in the transverse plane proceeds to the second selective $90°_x$, 50% of the signal will be unaffected by the second pulse, remaining transverse and consequently crushed, similar to STEAM (10). This loss is prevented by applying a "hard" $180°_x$ at time $\tau_1/2$:

$$\xrightarrow{180°_x} \mp[I_Y\cos(\frac{\Delta\omega\tau_1}{2}) + I_X\sin(\frac{\Delta\omega\tau_1}{2})]. \tag{3}$$

Allowing this magnetization to evolve for $\tau_1/2$ past, the $180°_x$, refocuses it to yield,

$$\mp [I_Y\cos(\frac{\Delta\omega\tau_1}{2}) + I_X\sin(\frac{\Delta\omega\tau_1}{2})] \xrightarrow{-\Delta\omega \frac{\tau_1}{2} I_Z} \mp I_Y. \tag{4}$$

This avoids both the formation of a stimulated echo and its 50% signal loss.

In the volume where the second T-HSI $90°_x$ intersects the first, the $\mp I_Y$s of Eq. [4] are converted to $\pm I_Z$ creating a two-dimensional "longitudinal," $\pm\mathbf{M_Z}$, Hadamard order, as shown in Figure 3b, immune to gradients during τ_2 (Fig. 2). This enables a very effective OVS during τ_2 as described in the following section. Although the $-\mathbf{M_Z}$s relax toward their equilibrium values, as $\tau_2 \ll T_1$, only minimal SNR loss is incurred but no localization errors are incurred(23). The third T-HSI $90°_x$ then encodes the VOI along a third direction nutating the $\pm I_Z$s to the transverse plane to be detected as a free induction decay (FID).

If, in addition to the $-\Delta\omega I_Z$ term of equations [2], a homonuclear J interaction, $\pi J_{12} I_{1Z} I_{2Z}$, exists between neighboring spins 1 and 2, the evolution due to it in the τ_1 interval will be,

$$\pm I_Y \xrightarrow{\pi J_{12} I_{1Z} I_{2Z}} \pm\left[I_{1Y}\cos\frac{\beta}{2} - 2I_{1X}I_{2Z}\sin\frac{\beta}{2}\right] \tag{5}$$

where$\beta = \pi J_{12}\tau_1$ and the effect of the $180°_x$ pulse has been neglected as it has no impact on evolution under coupling. The second $90°_x$ in Figure 2 will convert the magnetization in Eq. [5] to,

$$\xrightarrow{90°_x} \underbrace{\pm I_{1Z}\cos\frac{\beta}{2}}_{\text{Longitudinal}} \mp \underbrace{I_{1X}I_{2Y}\sin\frac{\beta}{2}}_{\text{Transverse}}. \tag{6}$$

Gradient pulses during τ_2 will crush "leftover" transverse components which could otherwise yield the up to five spin echoes (24). Only the longitudinal component, $\pm I_{1Z}\cos\frac{\beta}{2}$ in Eq. [6], remaining after τ_2, will be converted by the last T-HSI $90°_x$ to,

$$\xrightarrow{90°_x} \pm I_{1Y}\cos\frac{\beta}{2} \tag{7}$$

which is the detected FID. As J-coupled signals are weighted by both the $-\Delta\omega I_Z$ term of Eq. [2] and a $\cos\beta/2$ factor, β should be minimized by reducing τ_1 to as short as the hardware allows.

OVS

Following the first two T-HSI pulses, any leftover transverse magnetization outside the VOI is crushed (Figure 3a,b). Longitudinal magnetization at the VOI corners,
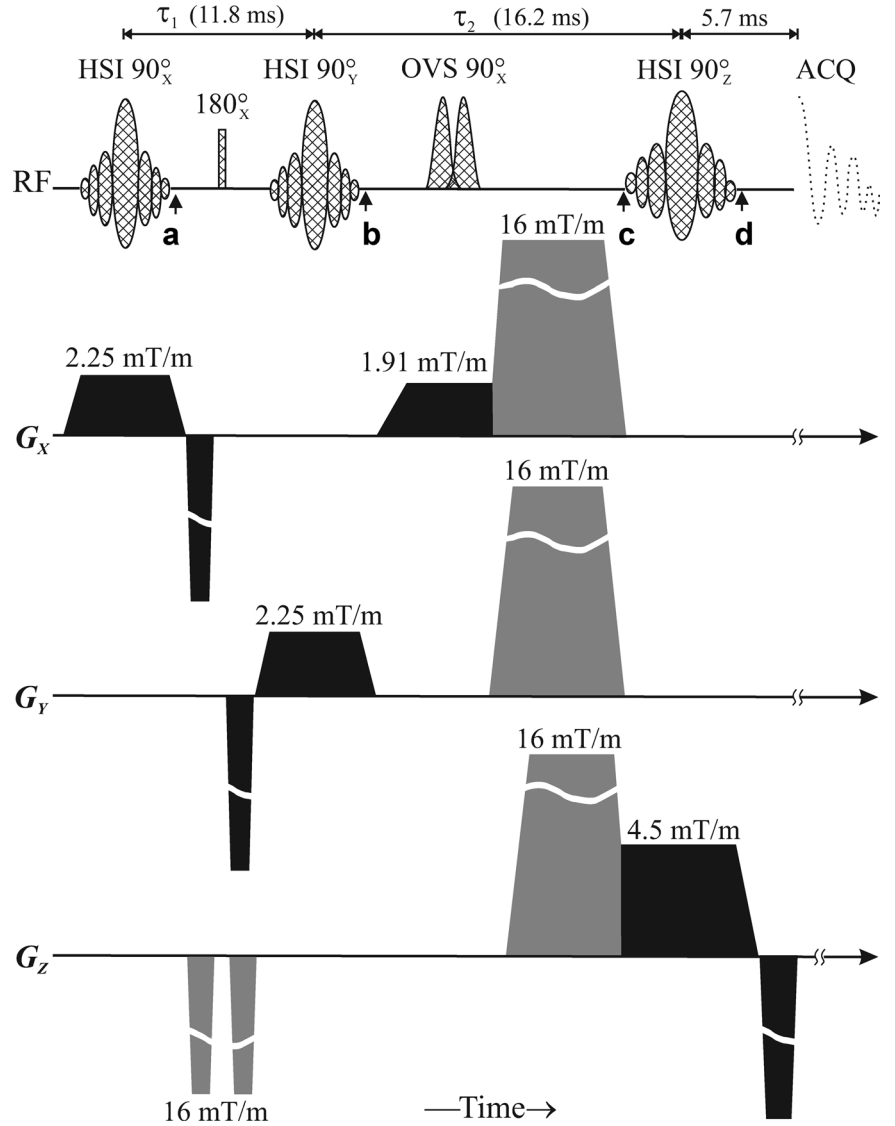
FIG. 2. The 3D T-HSI sequence. Selective 8.192 ms eigth-order T-HSI pulse in the LR (*X*) and AP (*Y*) directions, both under 2.25 mT/m were refocused by 1 ms gradient pulses, to minimize τ_1. A 0.5 ms hard 180° at $\tau_1/2$ (=5.9 ms), refocuses all transverse magnetization as shown by Eq. [3]. A 5.12 ms dual-band selective OVS RF pulse then excites and crushes any magnetization outside the VOI during τ_2 = 16.2 ms. Finally, a third 8.192 ms fourth-order T-HSI 90° pulse under a 4.5 mT/m gradient along the IS (*Z*) completes the VOI definition and brings its magnetization to the transverse plane to be sampled immediately. The magnetization at points **a, b, c,** and **d**, is shown schematically in Figure 3.

however, is unaffected by these pulses, as shown in Figure 3c, and will be Hadamard-encoded by the third (Fig. 3d) to contaminate the VOI. Two methods are combined to suppress this. First, a phase cycling scheme reverses the phase of the last two T-HSI pulses at odd averages. This does not affect the magnetization in the VOI that experiences all three T-HSI pulses, as shown in Fig. 3d. Summing odd and even acquisitions destructively interferes these unwanted signals, as shown in Figure 3e.

Additional OVS is achieved with a 5.12 ms dual-band Shinnar-Le-Roux 90° pulse (25), before the last T-HSI 90°s, when the VOI magnetization is longitudinal and immune to gradients, as shown in Figures 2 and 3c. It excites two 8 cm wide bands on both sides of the VOI (Fig. 3c) during τ_2, leaving the lipids only ~ 10 ms to recover compared with 30–40 ms when OVS is applied before VOI definition. This difference is significant given the lipids' short, ~ 200 ms T_1s. The longitudinal VOI magnetization, affected only by T_1 during τ_2, will suffer <1% loss in sensitivity and none in localization, given metabolites' long, >1 s, T_1s (26,27).

METHODS

Human Subjects

A healthy 28-year-old male volunteer and a healthy 34-year-old female were recruited for this study. Their "healthy" status was determined based on self-reporting negative answers to a questionnaire enumerating neurological disorders before the scan and MRI deemed "unremarkable" by a neuroradiologist afterward. The subjects gave Institutional Review Board approved written informed consent.

Simulation

Every *N*th order T-HSI pulse was synthesized by a superposition of *N* sincs, each apodized with a Hann filter and frequency shifted to excite the correct spatial location with a 0°, or 180° phase according to the +1 or −1 entry in that position in the corresponding row of $\mathbf{H}_N$. This process was repeated for each of the *N* rows of $\mathbf{H}_N$. The resulting slice profiles for these pulses, $L_p(\omega)$ of
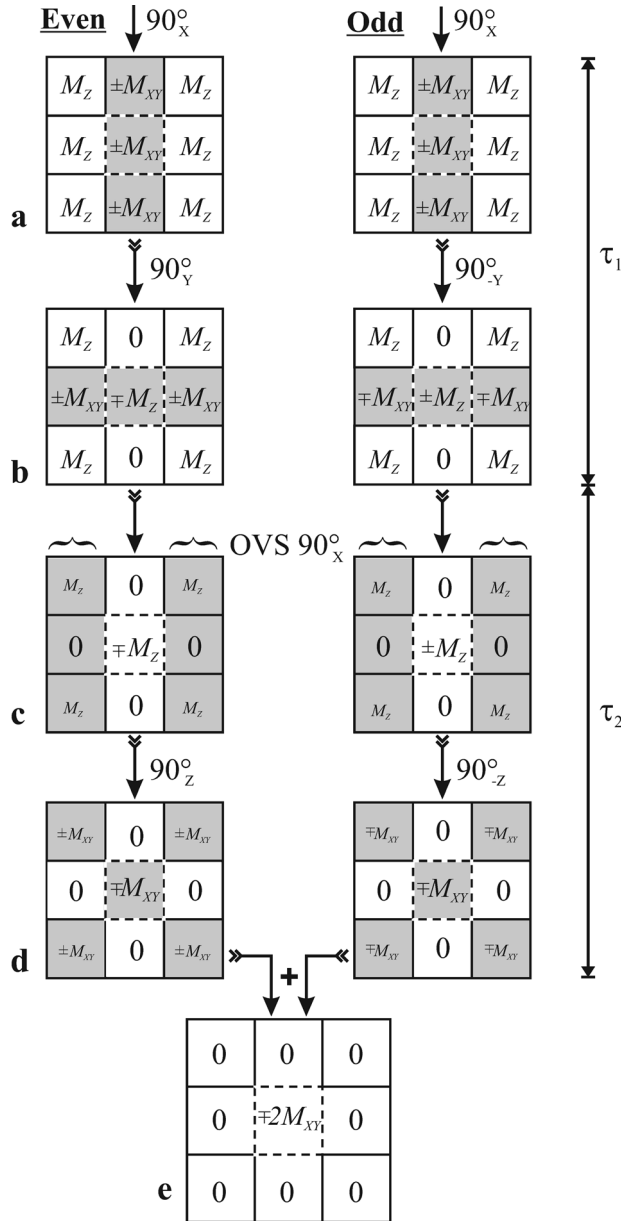
FIG. 3. The OVS scheme: the dashed rectangle in the center indicates the VOI and all others represent the sample's outside. Shading indicates regions excited by the preceding RF pulses. The **a**, **b**, **c**, **d** indices correspond to the time points indicated in Figure 2. The braces indicate regions excited by the OVS pulse. A phase cycling scheme that consists of inverting the phase of the last two HSI pulses (**a, c**) at odd acquisitions ensures that spins inside the VOI are unaffected. Spins outside the VOI are inverted at odd iterations (**d**). Summation of the two measurements eliminates the extraneous signals (**e**).

Eq. [1], under a constant 2.25 mT/m gradient were simulated by numerically solving the Bloch equations in the presence of relaxation ($T_1/T_2 = 1$ s/250 ms), using in-house software (MATLAB, The Mathworks Inc., Natick, MA).

Phantom

SNR and localization performance comparison of T-HSI versus CSI was done in a cylindrical phantom comprising four circular 152×17 mm diameter $\times$ thickness (including a 3.0 mm wall) partitions, submerged in water to reduce the air-water susceptibility, as shown in Figure 4a. Each compartment was spatially "labeled" with 100 mM (in protons) solution of a different metabolite yielding a singlet at a distinct chemical shift: Methanol (Meth), Na-acetate (NaAc), tert-butanol (*t*-But), and Tri-methyl-silyl propanoic acid (TMSP) at 3.4, 1.9, 1.2, and 0.0 ppm.

MRI

All experiments were done in a 1.5-T whole-body imager using its transmit-receive head-coil (Magnetom Avanto, Siemens AG, Erlangen Germany). Axial T_1-weighted magnetization prepared rapid gradient echo (MP-RAGE): TE/inversion time/TR = 3.79/1100/2100 ms, 256×256 matrix, 220×220 mm^2 FOV, 208 1 mm thick slices, MRI were obtained and reformatted into axial, sagittal, and coronal projections at 1 mm^3 isotropic resolution for VOI image-guidance.

3D T-HSI

At TR = 1.2 s, optimal for ~ 1 s T_1s of brain metabolites (28), the $8 \times 8 \times 4 = 256$ encoding steps $\times 2$ phase cycles $\times 2$ averages $= 1024$ acquisitions took 21 min. A 1.9 kHz peak $\mathbf{B_1}$ satisfied both the voltage and 3.2 W kg^{-1} SAR limits in the head (19). This $\mathbf{B_1}$ and VOI size dictated 2.25 and 4.5 mT/m selective gradients along the $\times 8$ and $\times 4$ directions (Fig. 2) leading to 0.08 and 0.04 cm (8 and 4%) of the slice thickness maximum chemical shift displacement between *N*-acetyl aspartate (NAA) and choline (Cho). The FIDs were sampled for 512 ms at ± 500 Hz bandwidth starting 5.7 ms from the center of the last pulse, as shown in Figure 2.

The MRSI data were processed off-line with our custom software. Residual water signals were removed from each FID (29). The data was then Fourier transformed in the time domain and 3D inverse Hadamard transformed along all three spatial directions (30). Each spectrum was automatically corrected for frequency, zeroth and first order phase shift (arising from the delay in the FID acquisition due to the refocusing gradient) using the NAA and Cho peaks as references.

HSI Versus CSI Comparison

A 1D version of the proposed sequence was run on the phantom with a $5.5 \times 15 \times 15$ cm^3 VOI and $4 \times 1 \times 1$ (LR $\times$ AP $\times$ IS) resolution, as shown in Figure 4. The experiment was repeated using CSI-STEAM [mixing time (TM)/TE=16/20 ms] with $\times 4$ phase-encoding along the partitions and same resolution, VOI and 10 s TR. The same phantom position, sampling duration, and bandwidth were used for both experiments. To assess the reproducibility, each experiment was repeated nine times back-to-back. The $\times 4$ encodings $\times 2$ averages $\times 9$ repetitions = 72 acquisitions took 12 min.

In Vivo Reproducibility

To assess the reproducibility of the 3D T-HSI sequence in vivo, we repeated the acquisition back-to-back four

FIG. 4. The phantom used for quantifying voxel bleed and SNR (**a**) and the resulting spectra from the 4 × 1 × 1 CSI-STEAM (**b**) and HSI (**c**) sequences. The CSI-STEAM spectra have been scaled ×2-fold for visual comparison with the HSI. Arrows indicate interslice bleed. Note the bleed in CSI metabolites extends across the entire VOI whereas HSI's is significantly smaller and limited in extent (better localization) and the consequent higher SNR of the latter reflecting the smaller bleed (Table 1).
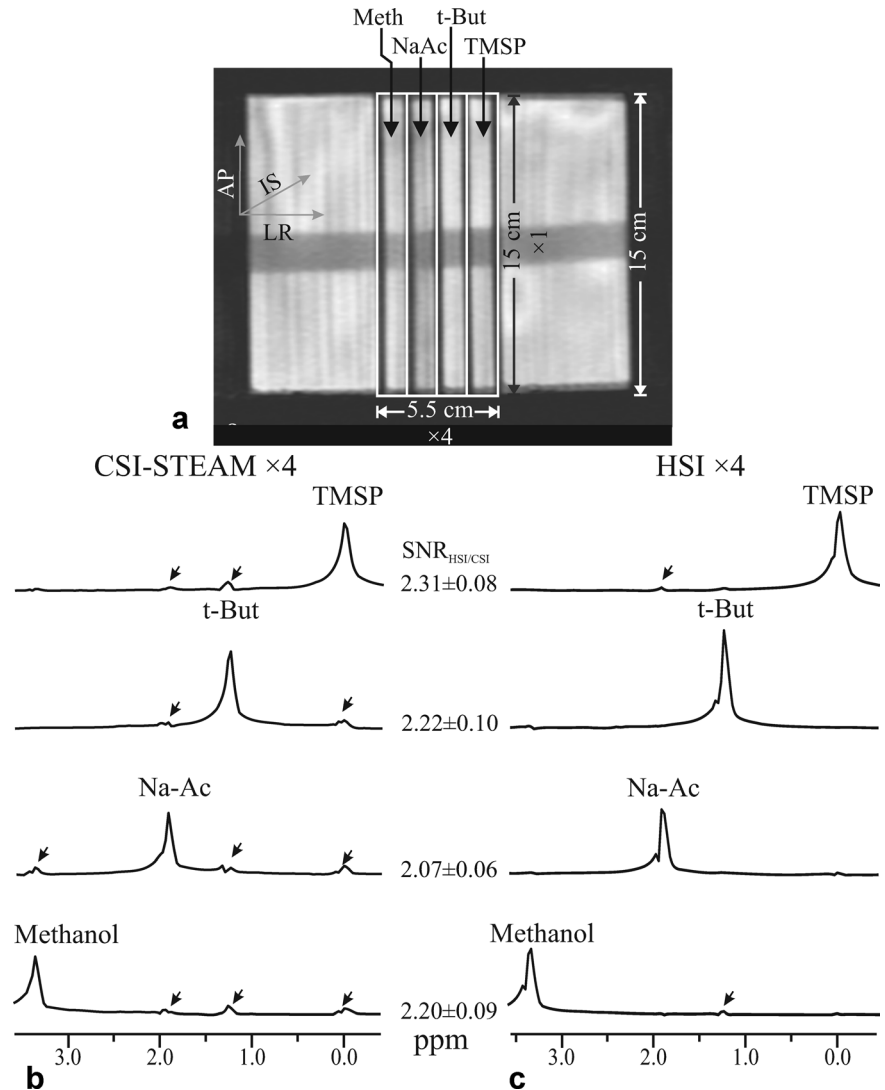
times on the same volunteer without moving or changing any of the acquisition parameters to avoid possible VOI misregistration and biological noise. A 3D localizer was performed between the sets to allow estimation of subject motion between scans.

RESULTS

Simulation

The simulated transverse magnetizations that are the results of the application of each Hadamard pulse on a homogeneous sample are shown in Figure 1a. Applying an inverse Hadamard transform (Eq. [1]) to them yields the individual slice profiles, shown in Figure 1b. Note the: (i) finite pulse length and gradient strength; (ii) imperfect individual pulses that excite regions outside of the voxel (marked with arrows in Fig. 1b) and which, therefore, do not cancel in the add-subtract inverse transform; and (iii) interaction between the superimposed individual SINCs used to synthesize the overall pulse, e.g., Bloch-Siegert shifts (31), all combine to cause a 6% slice profile deviation from ideal, calculated by taking their areas ratio.

Phantom

Automatic shimming yielded a 7 Hz VOI water linewidth. The VOI position was chosen so that each compartment contained one voxel, i.e., should yield a single spectral line at a unique chemical shift, as shown in Figure 4a. Additional lines would, therefore, indicate bleed, their chemical shift disclosing their partition of origin and their intensity indicating the bleed's amount. Given the VOI, resolution and 1 mm wall thickness of the compartments, they did not fully fill the 1.38 cm voxels used thus limiting the experimental bleed equally for both sequences.

Performance comparison of the T-HSI and CSI-STEAM sequences reveals less bleed for the former that is mostly confined to nearest neighbors, as shown in Figure 4b, reflecting its origin in the slice profile imperfections (Fig. 1b). The bleed for a given metabolite k, B_k, is estimated from its total peaks' areas in all compartments, T_k, and in its own compartment, S_k, as:

$$B_k = (T_k - S_k)/T_k \cdot 100\% \qquad [8]$$

The SNRs, defined as peak-height divided by the root mean square of the noise (32), along with its ratio for the

Table 1
SNR and Voxel Bleed (estimated according to Eq. [8]) Comparison Between ×4 CSI-STEAM and T-HSI from the Phantom in Figure 4

	Meth	NaAc	t-But	TMSP
SNR				
HSI	4451 ± 123	4035 ± 60	5947 ± 96	4885 ± 127
CSI	2023 ± 42	1946 ± 33	2679 ± 85	2117 ± 19
Bleed (%)				
HSI	14 ± 2.4	19 ± 1.0	12 ± 0.7	10 ± 0.6
CSI	20 ± 2.7	26 ± 2.3	23 ± 2.2	25 ± 2.3
Ratios				
$SNR_{HSI/CSI}$	2.20 ± 0.09	2.07 ± 0.06	2.22 ± 0.10	2.31 ± 0.08
$Bleed_{HSI/CSI}$	0.74 ± 0.13	0.75 ± 0.04	0.52 ± 0.03	0.40 ± 0.02

Note the correspondence between the substantially lesser bleed of HSI and the consequent better SNR, reflected by an $SNR_{HSI/CSI} > 2.0$.

two methods and their respective bleeds, are compiled in Table 1. The CSI results include loss due to voxel bleed and STEAM's inherent 50% loss (7,10).

In Vivo Human Brain

The position of the VOI is shown in Figure 5. Automatic shimming adjusted the first and second order currents to 17 Hz water linewidth in the VOI. The resultant 3D T-HSI spectra, shown in Figure 5, reflect the underlying anatomy, e.g., reduced (no) signals in voxels which partially (entirely) involve ventricles (5). Note that extraneous contamination that may arise from RF pulse imperfections (Fig. 1b), may excite spins outside the VOI. Although the imperfections are small (∼ 2%), the much larger extraneous volume they affect and high lipids' signals there can yield contamination much larger than the 1 cm^3 voxels metabolites' signals. These extraneous signals destructively interfere in reconstruction by the properties of the Hadamard matrix in all but its first, all +1s, row (21). Depending on the intensity of these signals, in a 3D T-HSI experiment, the first row, column and slice may need to be discarded, as shown in Figure 5, leaving $7 \times 7 \times 3 = 147$ usable spectra. The remaining voxels' average NAA, Cho, and Creatine (Cr) SNRs were: 31 ± 10, 23 ± 9, and 20 ± 8.

In Vivo Reproducibility

The area of the NAA, Cho, and Cr lines was integrated for every voxel in each of the four back-to-back experiments. Their mean and standard deviation were then used to estimate their coefficient of variation (coefficient of variation = standard deviation/mean) in each of the 147 voxels. The coefficient of variations' distributions are shown in Figure 6. The 20, 21, and 34% average coefficient of variations for NAA, Cr, and Cho are in line with those reported for MRSI in voxels of this size at 1.5 and 3 T (33–35). The localizer scans performed between each of the back-to-back scans showed less than 3 mm subject motion.

DISCUSSION

The twin requirements from any MRSI methodology are for spatial localization and SNR, given the dependence of the sensitivity and reproducibility on them (36–38). Implicit in the first requirement is confidence that the

signal in any given voxel (i) truly represents only the tissue in that voxel; (ii) does not contaminate its neighbors. These requirements motivated our two testable hypotheses: (i) that T-HSI offers better localization, reflected by less signal bleed; and, therefore, (ii) since the spins' signal energy is fixed, that it yields better voxel SNR compared with CSI using identical acquisition parameters: FOV, voxel size, acquisition time, and spatial resolution. Our findings (Table 1 and Fig. 4), substantiate both, specifically.

Localization

The T-HSI sequence shows 3–15% better SNR than the CSI. The expression for the PSF of CSI predicted the bleed to be ∼ 26% for each metabolite (3), similar to the 19–25% observed. The bleed in T-HSI was smaller than either the observed or theoretical bleed of CSI, reflecting its better signal localization. While it is noteworthy that several methods have been proposed to correct for the PSF of CSI either in postprocessing (39) or during RF excitation (40); the former unfortunately reduce the spatial resolution or prolong scan time, whereas the latter are yet to be demonstrated in the brain.

A second facet of localization is relative immunity to contaminating signals from outside the VOI. Because of the relative similarity of brain tissue signal, this is most apparent when skull lipids appear in a VOI that should not contain any. Absence of lipid peaks in the 1.3 ppm region in the spectra in Figure 5 demonstrates the effectiveness of the proposed sequence and obviates the need for spin-echo definition of the VOI. The fact that the bleed of T-HSI inside the VOI is largely limited to nearest neighbors and (contrary to CSI) does not extend across the FOV, renders this sequence better suited to various clinical scenarios. For example, the presence of an elevated Cho signal away from a tumor mass can be used to reliably determine the extent of its infiltration rather than be an error representing bleed that results from the spatial encoding method (41).

SNR

The finite pulse lengths and the linear combinations of the magnetization due to the Hadamard transform dictated slice profiles that deviate from an ideal rectangle. Indeed, our 8.192 ms RF pulses are associated with a

FIG. 5. Left: Axial (**a**), coronal (**b**), and sagittal (**c**) MRI of the volunteer superimposed with the ^{1}H-MRSI VOI (solid white frame). Bottom, **d**: The real part of the 8 × 8 (LR × AP) ^{1}H spectra matrix from the VOI in **a**, on a common frequency (1.4–3.8 ppm) and intensity scales, along with the line and column discarded due to outside contamination as explained in the Results section. Voxels involving mostly ventricles are marked by dashed outline. The two rectangle-enclosed spectra in (**d**), corresponding to the regions in **a**, are magnified for better visualization of the smaller amplitude metabolites. Note the spectral resolution and SNR in these 1.0 cm³ voxels obtained in ∼ 20 min at 1.5 T and the lack of lipids signals in the 1.0–1.3 ppm range, as well as presence of short T_2 metabolites, e.g., *myo*-Inositol (mI) reflecting the non-spin-echo nature of the sequence.
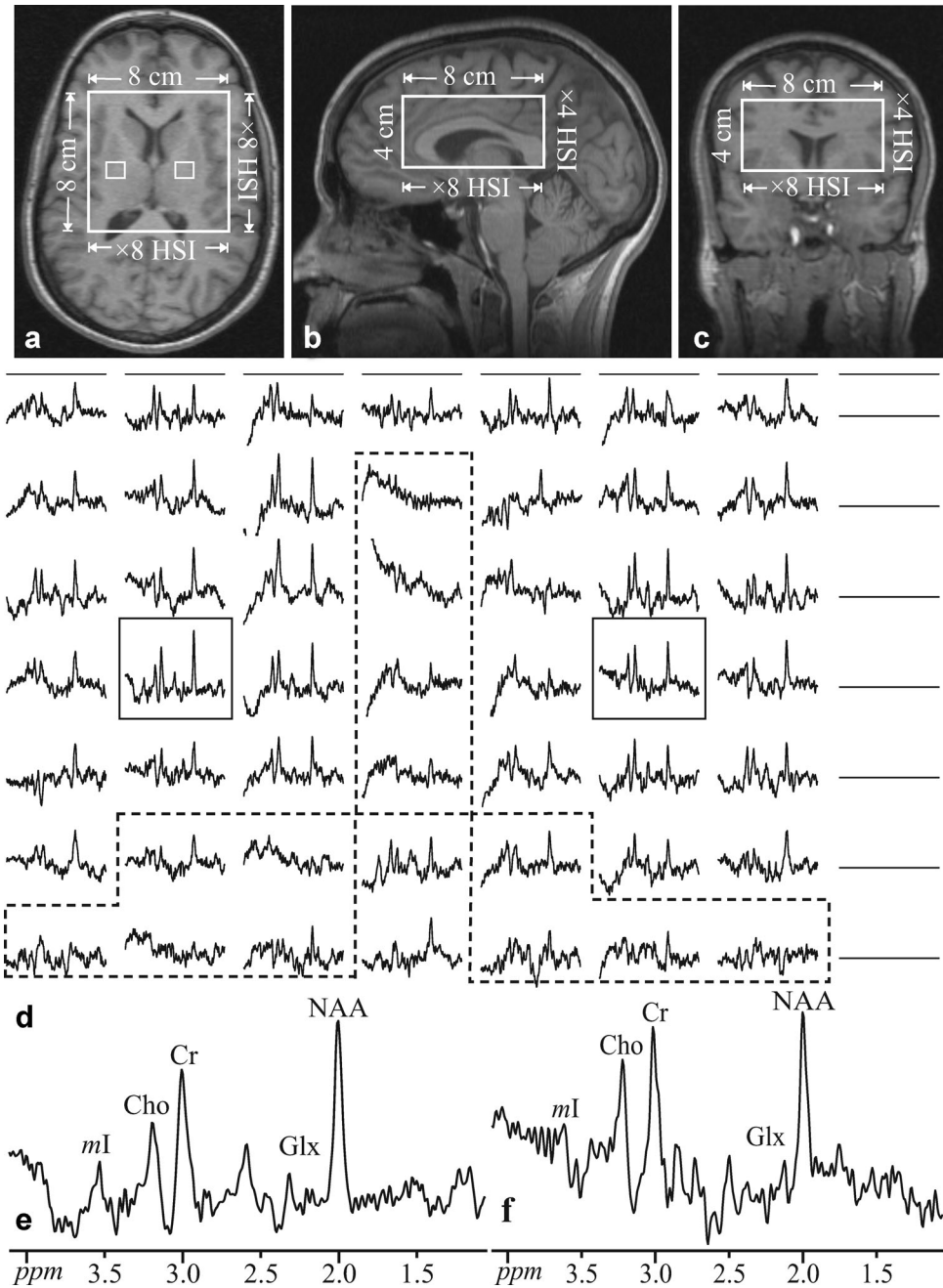
122 Hz transition band. Together with the 1.91 kHz peak RF power that restricted the selective gradients to 3.27 mT/m (1.39 kHz/cm) this led to a ∼ 4% signal loss compared with an ideal profile for our 1.38 cm wide voxels as obtained by simulation. The T-HSI bleed (Eq. [8]) was calculated based on the observed, 4% reduced signal. Taken together, both sources of loss (slice profile and bleed) result in ∼ 17% smaller signal compared with an ideal PSF of "1" inside the voxel and "0" everywhere outside. Comparing the ratio between the remaining signal in T-HSI (83% of ideal) and CSI (74%) yields the net 3–15% SNR gain for HSI compared with CSI reported in Table 1, substantiating the relationship between the PSF and SNR and excluding other loss mechanisms. Based

on the 1D experiment it is expected that the SNR gain will be even larger, 9–61%, in the 3D T-HSI encoding case.

Comparison with Short TE Spectra

The presence of short T_2 metabolites in Figure 5, e.g., glutamine, glutamate, and *myo*-inositol, is indicative of the non-spin-echo nature of the method and is in line with other ultra-short TE acquisitions (42,43). Furthermore, the reproducibility of the proposed sequence is similar to that obtained with CSI based methodology (33), demonstrating the equivalency of the T-HSI approach with regard to that clinically important criterion.
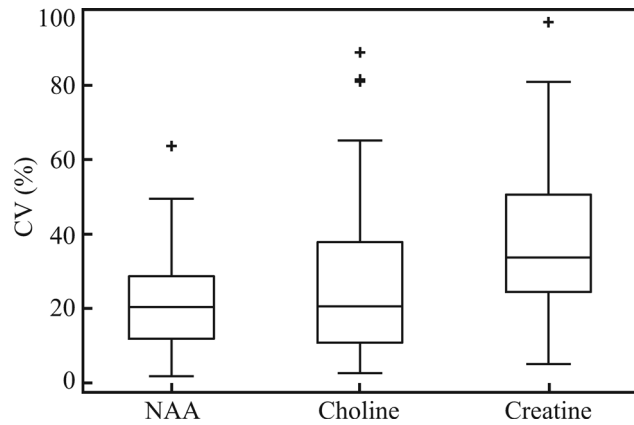
FIG. 6. Box plots showing the first, second (median), and third quartiles (box), $\pm 95\%$ (whiskers) and outliers ($+$) of the coefficient of variation for the three major metabolites in the VOI. Note the coefficient of variation means: 20, 21, and 34% for the NAA, Cho, and Cr at 1.5 T, are in line with similar size voxels at 3 T (33).

Limitations

The T-HSI pulses in this sequence are superpositions of N single-slice components making its peak amplitude $\times N$ higher. Staying within the coil's voltage breakdown limits restricts their selective gradients amplitude, thereby increasing the chemical shift displacement, as well as impacting the slice profiles and voxel bleed. As the available $\mathbf{B_1}$ per unit RF power decreases with magnetic field strength and the chemical shift displacement increases linearly with field, this method is more suitable to lower fields and smaller VOIs. As these issues depend on the RF pulse bandwidth that is in turn contingent on the hardware used, it can in principle be improved with better equipment as opposed to the PSF of CSI which is intrinsic. Additionally, the phase cycling scheme used for OVS doubles the minimum scan time. However, as multiple averages are required due to SNR considerations, scan times are typically greater than the minimum in any case. Further loss of signal occurs due to the delay caused by the 1 ms refocusing gradient of the third selective pulse, although it may be eliminated with the use of a self refocusing pulse. Finally, due to the properties of the Hadamard matrix, certain voxels may not reject extraneous signal contamination and need to be discarded (leaving $7 \times 7 \times 3$ from $8 \times 8 \times 4$ in this experiment). The impact of this loss, however, can be mitigated by judicious VOI placement.

CONCLUSIONS

As the spins in the entire VOI are excited and detected each acquisition, the method is theoretically optimal in SNR/unit-time (19,44). The extraneous signal rejection achieved by the selective pulses, destructive interference in the inverse Hadamard transform, and the OVS scheme, are sufficient for non-spin-echo acquisition, minimizing T_2 losses and J-modulations. With the ~ 10 minutes required for subject-loading, shimming and MRI, the procedure requires approximately 1/2 an hour, which can be tolerated by most. The RF waveforms used can be implemented on any modern imager and are on

the safe side with respect to their SAR. Finally, improved SNR and localization lend this method to clinical use, especially when smaller regions are of interest.

REFERENCES

1. Brown TR, Kincaid BM, Ugurbil K. NMR chemical shift imaging in three dimensions. Proc Natl Acad Sci USA 1982;79:3523–3526.
2. Maudsley A, Hilal S, Perman W, Simon H. Spatially resolved high-resolution spectroscopy by"four-dimensional" NMR. J Magn Reson 1983;51:147–152.
3. Brown T. Practical applications of chemical shift imaging. NMR Biomed 1992;5:238–243.
4. Shungu DC, Glickson JD. Sensitivity and localization enhancement in multinuclear in vivo NMR spectroscopy by outer volume presaturation. Magn Reson Med 1993;30:661–671.
5. Duyn JH, Gillen J, Sobering G, van Zijl PC, Moonen CT. Multisection proton MR spectroscopic imaging of the brain. Radiology 1993;188:277–282.
6. Spielman DM, Pauly JM, Macovski A, Glover GH, Enzmann DR. Lipid-suppressed single- and multisection proton spectroscopic imaging of the human brain. J Magn Reson Imaging 1992;2:253–262.
7. Maudsley A. Sensitivity in Fourier imaging. J Magn Reson 1986;68:363–366.
8. Ebel A, Govindaraju V, Maudsley AA. Comparison of inversion recovery preparation schemes for lipid suppression in 1H MRSI of human brain. Magn Reson Med 2003;49:903–908.
9. Bottomley PA. Spatial localization in NMR spectroscopy in vivo. Ann N Y Acad Sci 1987;508:333–348.
10. Frahm J, Merboldt KD, Hanicke W. Localized proton spectroscopy using stimulated echoes. J Magn Reson (1969) 1987;72:502–508.
11. Kok RD, van den Berg PP, van den Bergh AJ, Nijland R, Heerschap A. Maturation of the human fetal brain as observed by 1H MR spectroscopy. Magn Reson Med 2002;48:611–616.
12. Cho YD, Choi GH, Lee SP, Kim JK. (1)H-MRS metabolic patterns for distinguishing between meningiomas and other brain tumors. Magn Reson Imaging 2003;21:663–672.
13. Girard N, Fogliarini C, Viola A, Confort-Gouny S, Fur YL, Viout P, Chapon F, Levrier O, Cozzone P. MRS of normal and impaired fetal brain development. Eur J Radiol 2006;57:217–225.
14. Sibtain NA, Howe FA, Saunders DE. The clinical value of proton magnetic resonance spectroscopy in adult brain tumours. Clin Radiol 2007;62:109–119.
15. Frahm J, Michaelis T, Merboldt KD, Bruhn H, Gyngell ML, Hanicke W. Improvements in localized proton NMR spectroscopy of human brain. Water suppression, short echo times, and 1 ml resolution. J Magn Reson (1969) 1990;90:464–473.
16. McNab JA, Bartha R. Quantitative short echo-time 1H LASER-CSI in human brain at 4 T. NMR Biomed 2006;19:999–1009.
17. Henning A, Fuchs A, Murdoch JB, Boesiger P. Slice-selective FID acquisition, localized by outer volume suppression (FIDLOVS) for (1)H-MRSI of the human brain at 7 T with minimal signal loss. NMR Biomed 2009;22:683–696.
18. Fleysher L, Fleysher R, Liu S, Gonen O. Voxel-shift and interpolation for Hadamard-encoded MR images. Magn Reson Med 2008;60:524–535.
19. Gonen O, Arias-Mendoza F, Goelman G. 3D localized in vivo 1H spectroscopy of human brain by using a hybrid of 1D-Hadamard with 2D-chemical shift imaging. Magn Reson Med 1997;37:644–650.
20. Goelman G, Subramanian VH, Leigh JS. Transverse Hadamard spectroscopic imaging technique. J Magn Reson (1969) 1990;89:437–454.
21. Gonen O, Murdoch JB, Stoyanova R, Goelman G. 3D multivoxel proton spectroscopy of human brain using a hybrid of 8th-order Hadamard encoding with 2D chemical shift imaging. Magn Reson Med 1998;39:34–40.
22. Marshall AG. Fourier, Hadamard, Hilbert transforms in chemistry. New York: Springer; 1982.
23. Goelman G, Leigh JS. Hadamard spectroscopic imaging technique insensitive to pulse imperfections. J Magn Reson Ser A 1993;105:78–81.

24. Hahn EL. Spin echoes. Phys Rev 1950;80:580.

25. Shinnar M. Reduced power selective excitation radio frequency pulses. Magn Reson Med 1994;32:658–660.

26. Brief EE, Whittall KP, Li DK, MacKay A. Proton T1 relaxation times of cerebral metabolites differ within and between regions of normal human brain. NMR Biomed 2003;16:503–509.

27. Ethofer T, Mader I, Seeger U, Helms G, Erb M, Grodd W, Ludolph A, Klose U. Comparison of longitudinal metabolite relaxation times in different regions of the human brain at 1.5 and 3 Tesla. Magn Reson Med 2003;50:1296–1301.

28. Goelman G, Liu S, Hess D, Gonen O. Optimizing the efficiency of high-field multivoxel spectroscopic imaging by multiplexing in space and time. Magn Reson Med 2006;56:34–40.

29. Marion D, Ikura M, Bax A. Improved solvent suppression in one-and two-dimensional NMR spectra by convolution of time-domain data. J Magn Reson 1989;84:425–430.

30. Gonen O, Hu J, Stoyanova R, Leigh JS, Goelman G, Brown TR. Hybrid three dimensional (1D-Hadamard, 2D-chemical shift imaging) phosphorus localized spectroscopy of phantom and human brain. Magn Reson Med 1995;33:300–308.

31. Bloch F, Siegert A. Magnetic resonance for nonrotating fields. Phys Rev 1940;57:522.

32. Ernst RR, Bodenhausen G, Wokaun A. Principles of nuclear magnetic resonance in one and two dimensions. Oxford, UK: Clarendon Press Oxford; 1987.

33. Kirov, II, George IC, Jayawickrama N, Babb JS, Perry NN, Gonen O. Longitudinal inter- and intra-individual human brain metabolic quantification over 3 years with proton MR spectroscopy at 3 T. Magn Reson Med 2012;67:27–33.

34. Li BS, Babb JS, Soher BJ, Maudsley AA, Gonen O. Reproducibility of 3D proton spectroscopy in the human brain. Magn Reson Med 2002; 47:439–446.

35. Marshall I, Wardlaw J, Cannon J, Slattery J, Sellar R. Reproducibility of metabolite peak areas in ^{1}H MRS of brain. Magn Reson Imaging 1996;14:281–292.

36. Kreis R, Slotboom J, Hofmann L, Boesch C. Integrated data acquisition and processing to determine metabolite contents, relaxation times, and macromolecule baseline in single examinations of individual subjects. Magn Reson Med 2005;54:761–768.

37. Wiedermann D, Schuff N, Matson GB, Soher BJ, Du AT, Maudsley AA, Weiner MW. Short echo time multislice proton magnetic resonance spectroscopic imaging in human brain: metabolite distributions and reliability. Magn Reson Imaging 2001;19: 1073–1080.

38. Soher BJ, Maudsley AA. Evaluation of variable line-shape models and prior information in automated 1H spectroscopic imaging analysis. Magn Reson Med 2004;52:1246–1254.

39. Parker DL, Gullberg GT, Frederick PR. Gibbs artifact removal in magnetic resonance imaging. Med Phys 1987;14:640–645.

40. Panych LP, Zhao L, Mulkern RV. PSF-choice: a novel MRI method for shaping point-spread functions in phase-encoding dimensions. Magn Reson Med 2005;54:159–168.

41. Miller BL, Chang L, Booth R, Ernst T, Cornford M, Nikas D, McBride D, Jenden DJ. In vivo 1H MRS choline: correlation with in vitro chemistry/histology. Life Sci 1996;58:1929–1935.

42. Majors A, Xue M, Ng TC, Modic MT. Short echo time proton spectroscopy of human brain using a gradient head coil. Magn Reson Imaging 1992;10:649–654.

43. Seeger U, Klose U, Seitz D, Nagele T, Lutz O, Grodd W. Proton spectroscopy of human brain with very short echo time using high gradient amplitudes. Magn Reson Imaging 1998;16:55–62.

44. Posse S, Schuknecht B, Smith ME, van Zijl PC, Herschkowitz N, Moonen CT. Short echo time proton MR spectroscopic imaging. J Comput Assist Tomogr 1993;17:1–14.